Optimum Image Formation for Spaceborne Microwave Radiometer Products

David G. Long, *Fellow, IEEE*, and Mary J. Brodzik

Abstract—This paper considers some of the issues of radiometer brightness image formation and reconstruction for use in the NASA-sponsored Calibrated Passive Microwave Daily Equal-Area Scalable Earth Grid 2.0 Brightness Temperature Earth System Data Record project, which generates a multisensor multidecadal time series of high-resolution radiometer products designed to support climate studies. Two primary reconstruction algorithms are considered: the Backus–Gilbert approach and the radiometer form of the scatterometer image reconstruction (SIR) algorithm. These are compared with the conventional drop-in-the-bucket (DIB) gridded image formation approach. Tradeoff study results for the various algorithm options are presented to select optimum values for the grid resolution, the number of SIR iterations, and the BG gamma parameter. We find that although both approaches are effective in improving the spatial resolution of the surface brightness temperature estimates compared to DIB, SIR requires significantly less computation. The sensitivity of the reconstruction to the accuracy of the measurement spatial response function (MRF) is explored. The partial reconstruction of the methods can tolerate errors in the description of the sensor measurement response function, which simplifies the processing of historic sensor data for which the MRF is not known as well as modern sensors. Simulation tradeoff results are confirmed using actual data.

Index Terms—Brightness temperature, climate data record, Earth system data record, passive microwave remote sensing, radiometer, reconstruction, sampling, variable aperture.

I. INTRODUCTION

SATELLITE passive microwave observations of surface brightness temperature are critical to describing and understanding Earth system hydrologic and cryospheric parameters that include precipitation, soil moisture, surface water, vegetation, snow water equivalent, sea-ice concentration, and sea-ice motion. These observations are available in two forms: swath (sometimes referred to as NASA EOSDIS Level 1A or Level 1B) data and gridded (Level 3) data [1]. While swath data have applications for processes with short timescales, gridded data are valuable to researchers interested in derived parameters at fixed locations through time and are widely used in climate studies. Both swath and gridded data from the current time series of satellite passive microwave data sets span over 30 years of Earth observations, beginning with the Nimbus-7 Scanning Multi-channel Microwave Radiometer (SMMR) sensor in 1978, continuing with the Special Sensor Microwave/Imager (SSM/I) and Special Sensor Microwave Imager/Sounder (SSMIS) series sensors from 1987 onward, and including the completed observational record of Aqua Advanced Microwave Scanning Radiometer-Earth Observing System (AMSR-E) from 2002 to 2011. Although there are variations between sensors, this data record is an invaluable asset for studies of climate and climate change.

A number of heritage gridded products are available, including those from the National Snow and Ice Data Center (NSIDC) (see [2]–[4]). Although widely used in a variety of scientific studies, the processing and spatial resolution of existing gridded data sets are inconsistent, which complicates long-term climate studies using them. Each of the currently available gridded data sets suffers from inadequacies as Earth System Data Records [ESDRs, also referred to as Climate Data Records (CDRs)] since most of them were developed prior to the establishment of formal definitions for ESDR/CDRs. Perhaps, the most critical limitation of heritage products is the lack of cross-calibration of the sensors. In addition, all of the existing gridded data sets at NSIDC employ the original EASE-Grid projection [5], which has since been revised to be used more easily with standard geospatial mapping programs [6], [7]. Furthermore, since definition of these heritage products, new image reconstruction and interpolation schemes have been developed, which can be used to improve the products.

The SSM/I-SSMIS swath data record has been recently reprocessed and cross-calibrated by two research teams who have published the data as fully vetted fundamental CDRs (FCDRs): Remote Sensing Systems (Santa Rosa, CA) [8] and Colorado State University [9]. To exploit the availability of these new FCDRs and improved gridding schema while ameliorating the limitations of current gridded data sets, the NASA MEaSUREs Calibrated Passive Microwave Daily Equal-Area Scalable Earth (EASE) Grid 2.0 Brightness Temperature (CETB) Earth System Data Record (ESDR) [10] is generating a single consistently processed multisensor ESDR of Earth-gridded microwave brightness temperature (T_B) images. The multi-decadal product includes sensor data from SMMR, SSM/I, SSMIS, and AMSR-E with all the improved swath data sensor calibrations recently developed, as well as improvements in cross-sensor calibration and quality checking, modern file formats, better quality control, improved grid projection

definitions [6], [7], improved gridding techniques, and local-time-of-day (ltod) processing. To exploit developments in resolution enhancement, the CETB ESDR includes both conventional and enhanced resolution products. Designed to serve the land surface and polar snow/ice communities, the new products are intended to replace existing heritage gridded satellite passive microwave products with a single consistently processed ESDR [10].

A key part of processing is conversion of the swath-based measurements to the Level 3 grid. Algorithms to transform radiometer data from swath to gridded format are characterized by a tradeoff between noise and spatial and temporal resolution. Conventional drop-in-the-bucket (DIB) techniques provide low-noise low-resolution products, but higher resolution (with potentially higher noise) products are possible using image reconstruction techniques. By providing products with both processing options, users can compare and choose which option better suits their particular research application. The purpose of this paper is to explore the options for the high-resolution processing products and to compare the results to conventional resolution processing. A key goal of this paper is to describe the methods and their tradeoffs.

This paper is organized as follows. After some brief background, a review of the theory of radiometer image reconstruction is provided that includes a derivation of the radiometer measurement spatial response function (MRF) and a discussion of radiometer image formation algorithms. The succeeding section employs simulation to select the optimum parameters for image formation for the SSM/I sensor and to evaluate the sensitivity of the reconstruction to the accuracy of the response function. Actual data results are provided in the following section, followed by a summary conclusion. An Appendix considers the spatial frequency response of a radiometer MRF.

II. BACKGROUND

Previous gridded passive microwave data sets have used various swath-to-grid interpolation schemes on different grids for different radiometer channels. Some products [11] used classic DIB methods described in Section IV-A, whereas others [2], [3] used inverse-distance squared weighting. These approaches resulted in low-resolution gridded data with low noise, at the expense of spatial resolution. However, there is interest in the user community for higher resolution products.

For the conventional-resolution CETB product, all radiometer channels are gridded to a single coarse resolution grid using DIB method described in Section IV-A. To also provide a high spatial resolution product, the CETB exploits the results of previous studies that have demonstrated that high-resolution radiometer images can be produced using processing algorithms based on the Backus–Gilbert (BG) [12], [13] approach [14]–[18] and the radiometer form of the scatterometer image reconstruction (SIR) algorithm [19], [20], which has been successfully applied to SMMR, SSM/I, and AMSR-E data [19], [21].

BG was employed in generating the swath-based gridded SSM/I Pathfinder EASE-Grid product [4]. The BG implementation used data from a single swath even when overlapping swaths were available. Using a single swath reduces processing requirements by enabling precalculation of BG weights versus scan position, with tuning parameters set for low noise (and therefore low spatial resolution). The antenna footprints were assumed circular. Gridded data were produced separately for ascending and descending passes.

The Brigham Young University Scatterometer Climate Pathfinder (SCP, www.scp.byu.edu) generated an enhanced-resolution passive microwave data set for selected periods of SSM/I and AMSR-E. Available from NSIDC [21], the SCP product uses the SIR algorithm to report T_B on finer spatial grids than possible with conventional processing. This product combines data from multiple passes using measurement ltod, which minimizes fluctuations in the observed T_B at high latitudes due to changes in physical temperature from daily temperature cycling. Two images per day are produced, separated by 12 hours (morning and evening), with improved temporal resolution, permitting resolution of diurnal variations [22]. The enhanced resolution gridded data are proving useful in a variety of scientific studies, e.g., in [23] and [24].

Both BG and SIR use regularization to tradeoff noise and resolution. While BG is based on least squares and depends on a subjectively chosen tradeoff parameter for regularization, SIR employs maximum entropy reconstruction with regularization accomplished by limiting the number of iterations and thereby only producing partial reconstruction. BG and SIR provide similar results, although SIR offers a computational advantage over BG [19]. Based on ongoing feedback from an early adopter community, the final CETB product will likely contain images derived from only one of the candidate image reconstruction methods. To inform this decision, one of the goals of this paper is to describe the methods and their tradeoffs.

A. LTOD

The passive microwave sensors employed in the CETB fly on near-polar sun-synchronous satellites, which maintain an orbital plane with an orientation that is (approximately) fixed with respect to the sun. Thus, the satellite crosses the equator on its ascending (northbound) path at the same ltod (within small tolerance). The resulting coverage pattern yields passes about 12 h apart in ltod at the equator. Most areas near the pole are covered multiple times per day. Analyzing the data from a single sensor, we find that polar measurements fall into two ltod ranges. The two periods are typically less than 4 h long and are spaced 8 or 12 h apart. Significantly, at any particular location, the orbital pass geometry causes the ltod of the observations to differ from day to day in a cyclic manner [22]. When not properly accounted for, this can introduce undesired variability (noise) into a time series analysis due to diurnal variations of the surface that is sampled at different ltod over the multiday orbit repeat cycle.

Heritage gridded T_B products have either 1) averaged all measurements during the day that fall in a given grid cell [11]; or 2) selected measurements from only one (ascending or descending) pass per day [2]–[4]. The observed microwave brightness temperature is the product of surface physical temperature and surface emissivity. Since surface temperatures can fluctuate
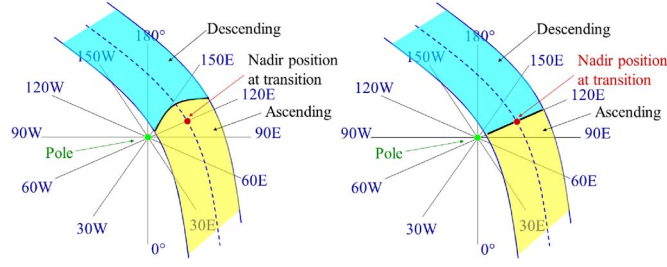
Fig. 1. Illustrations of the boundaries along the swath for (left) ascending/descending and (right) ltod for a northern hemisphere swath. The ascending/descending division is based on the nadir position of the spacecraft and, due to the antenna rotation, results in significant ltod spread between passes at the poles. The ltod approach segments the swath based on the ltod of each measurement and results in more consistent swath division.

widely during the day, daily averaging (method 1) is not generally useful since it smears diurnal temperature fluctuations in the averaged T_B. The single-pass approach (method 2) discards large amounts of potentially useful data. This method separates data into ascending pass-only and descending pass-only data, resulting in two images per day. This is a reasonable approach at low latitudes, but at higher latitudes, the ascending/descending division does not work as well since adjacent pixels along swath overlap edges can come from widely different ltod (which vary on subsequent days) [22]. The gridded field of T_B's, ostensibly all representing consistent ltods, actually represent different physical temperature conditions. Thus, some modified form of swath averaging is desired.

Another alternative is to split the data into two images per day, based on the ltod approach of Gunn and Long [22]. Fig. 1 shows the difference in where the ascending/descending division and ltod divisions occur. Particularly near the pole, the ltod approach ensures that all measurements in any one image have consistent spatial/temporal relationships. The CETB adopts the ltod division scheme for the northern and southern hemispheres. At low latitudes, (which typically have few overlapping swaths at similar ltod in the same day), the ltod division is equivalent to the ascending/descending division. For the CETB product, an ancillary image is included to describe the effective time average of the measurements combined into the pixel for a particular day. This enables investigators to explicitly account for the ltod temporal variation of the measurements included in a particular pixel. To account for the differences in orbits of the different sensors, the precise ltod division time for the twice-daily images varies among sensors.

III. RADIOMETER SPATIAL RESPONSE FUNCTION

The effective spatial resolution of gridded image products is determined by the MRF of the sensor and by the image formation algorithm used. The MRF is determined by the antenna gain pattern, which is unique for each sensor and sensor channel, and varies with scan angle, the scan geometry (notably the antenna scan angle), and the measurement integration period. This section derives the MRF for a microwave radiometer. First, basic background is provided, followed by a discussion of the effects of temporal integration.

A. Background Theory

Microwave radiometers measure the thermal emission, which is sometimes called Plank radiation, radiating from natural objects [25]. In a typical radiometer, an antenna is scanned over the scene of interest, and the output power from the carefully calibrated receiver is measured as a function of scan position. The reported signal is a temporal average of the filtered received signal power [25].

The observed power is related to receiver gain and noise figure, antenna loss, physical temperature of the antenna, antenna pattern, and scene brightness temperature. In simplified form, the output power P_{SYS} of the receiver can be written as [25]

$$P_{SYS} = kT_{SYS}B \tag{1}$$

where $k = 1.38 \times 10^{-23}$ (J/K) is Boltzmann's constant, B is the receiver bandwidth in hertz, and T_{SYS} is the system temperature in Kelvin with

$$T_{SYS} = \eta_l T_A + (1 - \eta_l)T_p + (L - 1)T_p + LT_{REC} \tag{2}$$

where η_l is the antenna loss efficiency (unitless), T_p is the physical temperature in Kelvin of the antenna and waveguide feed, L is the waveguide loss (unitless), T_{REC} is the effective receiver noise temperature (determined by system calibration) in Kelvin, and T_A is the effective antenna temperature in Kelvin. As described in the following, the effective antenna temperature is dependent on the direction the antenna points and on the scene characteristics. Since the other instrument-related terms (i.e., $(1 - \eta_l)T_p + (L - 1)T_p + LT_{REC}$) can be removed by proper calibration, the value of T_A, which depends on the geophysical parameters of interest, is thus estimated from T_{SYS}.

The effective antenna temperature T_A can be modeled as a product of the apparent temperature distribution $T_{AP}(\theta, \phi)$ in the look direction θ, ϕ, and the antenna radiation gain $F(\theta, \phi)$, which is proportional to the antenna gain pattern $G(\theta, \phi)$ [25]. T_A (in Kelvin) is obtained by integrating the product of apparent temperature distribution $T_{AP}(\theta, \phi)$ (in Kelvin) and the unitless antenna pattern $G(\theta, \phi)$:

$$T_A = G_a^{-1} \iint G(\theta, \phi)T_{AP}(\theta, \phi)d\theta d\phi \tag{3}$$

where

$$G_a = \iint G(\theta, \phi)d\theta d\phi \tag{4}$$

and $G(\theta, \phi)$ is the instantaneous antenna gain for the particular channel and where the integrals are over the range of values corresponding to the nonnegligible gain of the antenna. Note that the antenna pattern acts as a nonideal low-pass spatial filter of the surface brightness distribution, limiting the *primary* surface contribution to the observed T_B to approximately 3-dB beamwidth, although the observed value includes contributions from a larger area.

For downward-looking radiometers, the apparent brightness temperature distribution includes contributions from the surface

and from the intervening atmosphere [25]. For a spaceborne sensor, this can be expressed as

$$T_{\mathrm{AP}}(\theta, \phi) = [T_B(\theta, \phi) + T_{\mathrm{ss}}(\theta, \phi)] e^{-\tau \sec \theta} + T_{\mathrm{up}}(\theta) \quad (5)$$

where $T_B(\theta, \phi)$ is the surface emission brightness temperature, $T_{\mathrm{ss}}(\theta, \phi)$ is the surface scattered radiation, τ is the total effective optical depth of the atmosphere, and $T_{\mathrm{up}}(\theta)$ is the effective atmospheric upwelling temperature, which depends on the temperature and density profile, atmospheric losses, clouds, rain, etc.

Ignoring incidence and azimuth angle dependence, the surface brightness temperature is

$$T_B = \epsilon T_P \quad (6)$$

where ϵ is the emissivity of the surface, and T_P is the physical temperature of the surface. The emissivity is a function of the surface roughness and permittivity, which are related to the geophysical properties of the surface [25]. In geophysical studies, the ultimate key parameter of interest is typically ϵ, although T_P is also of interest.

The surface scattering temperature $T_{\mathrm{ss}}(\theta, \phi)$ is the result of downwelling atmospheric emissions that are scattered off of the rough surface toward the sensor. This signal depends on the scattering properties of the surface (surface roughness and dielectric constant) as well as the atmospheric emissions directed toward the ground. We note that, although some azimuth variation with brightness temperature has been observed over the ocean [26], sand dunes [27], and snow in Antarctica [28], vegetated and sea-ice-covered areas generally have little or no azimuth brightness variation [8].

B. Signal Integration

The received radiometer signal is very noisy. To reduce the measurement variance, the received signal power is averaged over a short integration period. Even so, the reported measurements are noisy due to the limited integration time available for each measurement. The uncertainty is expressed as ΔT, which is the standard deviation of the temperature measurement. ΔT is a function of the integration time and bandwidth used to make the radiometric measurement and is typically inversely related to the time–bandwidth product [25]. Increasing the integration time and/or bandwidth reduces ΔT. High stability and precise calibration of the system gain are required to accurately infer the brightness temperature T_B from the sensor power measurement P_{SYS}.

Because the antenna is scanning during the integration period, the effective antenna gain pattern of the measurements is a smeared version of the antenna pattern. In the smeared case, we replace G in (3) and (4) with the smeared version of the antenna, G_s, where

$$G_s(\theta, \phi) = T_i^{-1} \int G(\theta, \phi + \omega_r t) dt \quad (7)$$

with T_i being the integration period, ω_r being the antenna rotation rate, and the integral limits being 0 and T_i. Note that because T_i is very short, the net effect is primarily to widen

the main lobe. Nulls in the pattern tend to be eliminated and the sidelobes widened. The smeared antenna pattern varies somewhat for different antenna azimuth angles, although for simplicity, this effect is not considered in this paper.

For imaging the surface, we can concentrate on the pattern smearing at the surface. The smeared antenna pattern $G_s(\theta, \phi)$ at the surface at a particular time defines the MRF of the corresponding T_B measurement. Due to varying geometry, the MRF of different measurements may be slightly different. For example, the azimuth angle changes across the swath result in varying rotation angle of the MRF.

Note from (5) that $T_{\mathrm{AP}}(\theta, \phi)$ consists primarily of an attenuated contribution from the surface (i.e., T_B) plus scattered and upwelling terms. We note that the reported T_A values compensate or correct (to some degree) for these terms.

Let T_A' denote the corrected T_A measurement. It follows that we can rewrite (5) in terms of the corrected T_A and the surface T_B value as

$$T_A' = G_a^{-1} \iint G_s(\theta, \phi) T_B(\theta, \phi) d\theta d\phi. \quad (8)$$

We can express this result in terms of the surface coordinates x and y by noting that, for a given x, y location and time, the antenna elevation and azimuth angles can be computed (see the Appendix). Then

$$T_A' = G_b^{-1} \iint G_s(x, y) T_B(x, y) dx dy \quad (9)$$

where

$$G_b = \iint G_s(x, y) dx dy. \quad (10)$$

In surface coordinates, the MRF is defined as

$$\mathrm{MRF}(x, y) = G_b^{-1} G_s(x, y) \quad (11)$$

so that

$$T_A' = \iint \mathrm{MRF}(x, y) T_B(x, y) dx dy. \quad (12)$$

Thus, the measurements T_A' can be seen to be the integral of the product of the MRF and the surface brightness temperature. The nominal resolution of the T_B measurements is generally considered the size of the 3-dB response pattern of the smeared MRF. Image formation estimates $T_B(x, y)$ from the measurements T_A'.

IV. GRIDDING AND RECONSTRUCTION

Algorithms that generate 2-D gridded images from raw measurements are characterized by a tradeoff between noise and spatial resolution. Our goal is to estimate an image of the surface $T_B(x, y)$ from the sensor T_B measurements. The "nominal" resolution of the T_B measurements is typically considered the size of the 3-dB response pattern of the MRF. Although the effective resolution of DIB imaging is no finer

than the effective resolution of the measurements, reconstruction techniques can yield higher effective resolution if spatial sampling requirements are met.

As previously noted, the CETB project [10] is to produce both low-noise gridded data and enhanced-resolution data products. The low-resolution gridded data uses the DIB method described in the following. These products are termed "low resolution" or "nonenhanced resolution" and are denoted as gridded (GRD) products. Higher resolution products are also generated using one of the two image reconstruction methods: the radiometer form of the SIR algorithm or the BG image formation method, as described in the following. Unlike the approach taken for the historical EASE-Grid data [4], the CETB does not attempt to degrade the resolution of the highest channels to match the coarsest channel; rather, it independently optimizes the resolution for each channel in the high-resolution products. The product is Earth-located (in contrast to swath based) using EASE-Grid 2.0 [6], [7]. In generating CETB gridded data, only measurements from a single sensor and a channel are processed. Measurements combined into a single grid element may have different Earth azimuth and incidence angles (although the incidence angle variation is small). Measurements from multiple orbit passes over a narrow local time window may be combined. When multiple measurements are combined, the resulting images represent a temporal average of the measurements over the averaging period. There is an implicit assumption that the surface characteristics remain constant over the imaging period and that there is no azimuth variation in the true surface T_B. For both conventional (nonenhanced) resolution and enhanced-resolution images, the effective gridded image resolution depends on the number of measurements and the precise details of their overlap, orientation, and spatial locations.

The succeeding sections provide a brief summary of the algorithms used for image formation. Channels are gridded at enhanced resolution on nested grids at power-of-two relationships to the 25-km base grid. This embedded gridding simplifies overlaying grids from different resolutions. The method for determining the fine-resolution grid for each channel is given in the following.

A. Coarse-Resolution GRD Gridding Algorithm

A classic coarse-resolution gridding procedure is the simple DIB average. The resulting data grids are designated GRD data arrays. For the DIB gridding algorithm, the key information required is the location of the measurement. The center of each measurement location is mapped to an output projected grid cell. All measurements within the specified time period whose center locations fall within the bounds of a particular grid cell are averaged together. The unweighted average becomes the reported pixel value. Although some investigators [2], [3] have interpolated measurement locations to the center, or weighted the measurements by the distance to the center, such interpolation increases the noise level; therefore, in the CETB no interpolation or measurement weighting is done. CETB ancillary data contain the number and standard deviation of included samples.
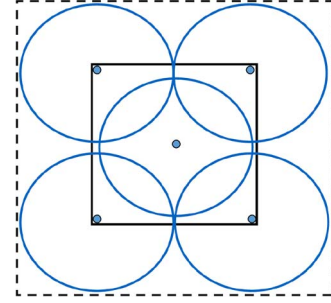

Fig. 2. GRD pixel resolution illustration. The inner square represents the pixel area while the 3-dB footprints of some potential measurements, whose center is shown as a dot, are placed within the pixel. Note that more than half of some measurement can extend outside the pixel area. Depending on the measurement distribution, to the first order, the dimensions of the effective pixel size are thus the sum of the pixel and the footprint dimensions as indicated by the dashed bounding box.

The effective spatial resolution of the GRD product is defined by a combination of the pixel size and spatial extent of the 3-dB antenna footprint size [19], [32] and does not require any information about the antenna pattern. Although the pixel size can be arbitrarily set, the effective resolution is, to the first order, the sum of the pixel size plus the footprint dimension (see Fig. 2). All CETB GRD products are produced on a 25-km pixel grid and thus have an effective resolution that is coarser than 25 km since the measurement footprints can extend outside of a pixel.

B. Reconstruction Algorithms

In the reconstruction algorithms, the effective MRF for each measurement is used to estimate the surface T_B on a fine-scale grid. The MRF is determined by the antenna gain pattern (which is unique for each sensor and sensor channel, and varies with scan angle), the scan geometry (notably the antenna scan angle), and the integration period. The latter "smears" the antenna gain pattern due to antenna rotation over the measurement integration period. The MRF describes how much the emissions from a particular receive direction contribute to the observed T_B value.

Denote the MRF for a particular channel by $R(\phi, \theta; \phi_i)$, where ϕ and θ are particular azimuth and elevation angles relative to the antenna boresite at azimuth scan angle ϕ_i. Note that, for a given antenna azimuth scan angle, the MRF is normalized so that the integral of the MRF over all azimuth and elevation angles is one.

Generally, for the FCDR data sets that are input to the CETB, the MRF can be treated as zero everywhere but in the direction of the surface. With this assumption, we can write $R(\phi, \theta; \phi_i)$ as $R(x, y; \phi_i)$, where x and y are the location (which we will express in map coordinates) on the surface corresponding to the azimuth and elevation angles for the particular ϕ_i. Note that $\int\int R(x, y; \phi_i) dx dy = 1$. A particular noise-free measurement T_i taken at a particular azimuth angle ϕ_i can be written as

$$T_i = \int\int R(x, y; \phi_i) T_B(x, y; \phi_i) dx dy \qquad (13)$$

where $T_B(x, y; \phi_i)$ is the nominal brightness temperature in the direction of point x, y on the surface as observed from the scan angle ϕ_i. Note that, if there is no significant difference in the atmospheric contribution as seen from different scan angles and if the surface brightness temperature is azimuthally isotropic, we can treat $T_B(x, y; \phi_i)$ as independent of ϕ_i so that $T_B(x, y; \phi_i) = T_B(x, y)$. $T_B(x, y)$ is referred to as the surface brightness temperature.

With this approximation, a typical brightness temperature measurement can be written as

$$T_i = \iint R(x, y; \phi_i) T_B(x, y) dx dy + \text{noise} \qquad (14)$$

where noise is radiometric measurement noise. Each measurement is seen to be the MRF-weighted average of T_B. The goal of the reconstruction algorithm is to estimate $T_B(x, y)$ from the measurements T_i.

For the problem at hand, T_B is desired at each sample point on the EASE-Grid 2.0 grid. While this is a regular grid, the measurement locations are not aligned with the grid, and the measurements form an irregular sampling pattern. There is a well-defined theory of signal reconstruction based on irregular sampling that can be applied to the problem [29], [31], [32]. However, since the signal measurements are quite noisy, full reconstruction can produce excessive noise enhancement. To reduce noise enhancement and resulting artifacts, at the expense of resolution, regularization can be employed [32]. Regularization is a smoothing constraint introduced to an inverse problem to prevent extreme values or overfitting.

The regularization in BG and SIR enable a tradeoff between signal reconstruction accuracy and noise enhancement. SIR is based on signal processing and treats the surface brightness temperature as a 2-D signal to be reconstructed from irregular samples (the measurements). BG is a least-squares approach that trades noise and solution smoothness using a subjectively selected parameter [12], [13]. While related alternate approaches exist [38], [39], [41], they are not considered here due to limited validation for this application and because their results are generally similar.

Both the BG and SIR approaches enable estimation of the surface brightness on a finer grid than is possible with the conventional DIB approaches, i.e., the resulting brightness temperature estimate has a finer effective spatial resolution than DIB methods. As a result, the results are often called "enhanced resolution," although in fact, the reconstruction algorithm merely exploits the available information to reconstruct the original signal at higher resolution than GRD gridding, based on the assumption of a bandlimited signal [20]. Compared with the GRD coarsely gridded product, the potential resolution enhancement depends on the sampling density and the MRF; however, improvements of 25% to 1000% in the effective resolution have been demonstrated in practice for particular applications. For radiometer enhancement, the effective improvement in resolution tends to be limited and in practice is typically less than 100% improvement. Nevertheless, the resulting images have improved spatial resolution and information. Note that to meet Nyquist requirements for the signal

processing, the pixel resolution of the images must be finer than the effective resolution by at least a factor of two.

For comparison, note that the effective resolution for DIB gridding is equivalent to the sum of pixel grid size plus the spatial dimension of the measurement, which is typically defined by the half-power or the 3 dB beamwidth. Based on Nyquist considerations, the highest representable spatial frequency for DIB gridding is twice the grid spacing.

Note that, in some cases (notably in the polar regions), multiple passes over the same area at the same ltod can be averaged together. Reconstruction algorithms intrinsically exploit the resulting oversampling of the surface to improve the effective spatial resolution in the final image.

C. Signal Reconstruction and SIR

In the reconstruction, $T_B(x, y)$ is treated as a discrete signal sampled at the map pixel spacing and is estimated from the noisy measurements T_i. The pixel spacing must be set sufficiently fine so that the generalized sampling requirements [30] are met for the signal and the measurements [20], [32]. Typically, this means that the pixel spacing must be one-half to one-tenth the size of antenna footprint size.

To briefly describe the reconstruction theory, for convenience, we vectorize the 2-D signal over an $N_x \times N_y$ pixel grid into a single-dimensional variable $a_j = T_B(x_j, y_j)$, where $j = l + N_x k$. The measurement equation (14) becomes

$$T_i = \sum_{j \in \text{image}} h_{ij} a_j \qquad (15)$$

where $h_{ij} = R(x_l, y_k; \phi_i)$ is the discretely sampled MRF for the ith measurement evaluated at the jth pixel center and the summation is over the image with $\sum_j h_{ij} = 1$. In practice, the MRF is negligible at some distance from the measurement; therefore, the sums need only to be computed over an area local to the measurement position. Some care has to be taken near image boundaries.

For the collection of available measurements, (15) can be written as the matrix equation, i.e.,

$$\vec{T} = \mathbf{H}\vec{a} \qquad (16)$$

where $\mathbf{H}$ contains the sampled MRF for each measurement, and $\vec{T}$ and $\vec{a}$ are vectors composed of the measurements T_i and the sampled surface brightness temperature a_j, respectively. Note that $\mathbf{H}$ is very large, sparse, and may be overdetermined or underdetermined depending on the sampling density. Estimating the brightness temperature at high resolution is equivalent to inverting (16). In the case of the CETB, H is typically underdetermined, and if explicitly written out, would have dimensions of over $10^6 \times 10^6$.

Due to the large size of $\mathbf{H}$, iterative methods are the most practical approach to inverting (16). One advantage of an iterative method is that regularization can be easily implemented by prematurely terminating the iteration; alternately, explicit regularization methods such as Tikhonov regularization [46] can be used.

The radiometer form of SIR is a particular implementation of an iterative solution to (16) that has proven effective in generating high-resolution brightness temperature images [19]. The SIR estimate approximates a maximum-entropy solution to an underdetermined equation and a least squares solution to an overdetermined system. The first iteration of SIR is termed "AVE" (for weighted average) and can be a useful estimate of the surface T_B. The AVE estimate of the jth pixel is given by

$$a_j = \frac{\sum_i h_{ij} T_i}{\sum_i h_{ij}} \qquad (17)$$

where the sums are over all measurements that have nonnegligible MRF at the pixel.

D. BG Method

A direct approach to inverting (16) is based on Backus and Gilbert [12], [13] who developed a general method for inverting integral equations. The BG method is useful for solving sampled signal reconstruction problems [33]. First applied to the radiometer data in [14], the BG method has been used extensively for extracting vertical temperature profiles from radiometer data [15]. It has also been used for spatially interpolating and smoothing data to match the resolution between different channels [40] and to improve the spatial resolution of surface brightness temperature fields [19], [34], [35]. Antenna pattern deconvolution approaches have also been attempted with varying degrees of success [44], [45].

In application to image reconstruction of the surface brightness temperature, the essential idea is to write an estimate of the surface brightness temperature at a particular pixel as a weighted linear sum of measurements that are collected "close" to the pixel. Using the notation developed earlier, the estimate at the jth pixel is

$$\widehat{a_j} = \sum_{i \in \text{nearby}} w_{ij} T_i \qquad (18)$$

where the sum is computed over nearby pixels and where w_{ij} are weights selected so that $\sum_i w_{ij} = 1$.

There is no unique solution for the weights; however, regularization permits a subjective tradeoff between the noise level in the image and the resolution [19]. Regularization and selection of the tuning parameters are described in detail elsewhere [33], [40]. There are two tuning parameters: an arbitrary-dimensional parameter and a noise-tuning parameter γ. The dimensional parameter affects the optimum value of tuning parameter γ. Following Robinson et al. [40], we set the dimensional-tuning parameter to 0.001. The noise-tuning parameter, which can vary from 0 to $\pi/2$, controls the tradeoff between the resolution and the noise. Varying γ alters the solution for the weights between a (local) pure least-squares solution and a minimum noise solution. The value of γ must be subjectively selected to "optimize" the resulting image and depends on the measurement noise standard deviation ΔT and the chosen penalty function. Following [35], we set the penalty function to a constant $J = 1$ and the reference function to $F = 1$ over the pixel of interest, and $F = 0$ elsewhere.

TABLE I
SSM/I CHANNEL CHARACTERISTICS [37]. MOST FREQUENCIES HAVE BOTH VERTICALLY POLARIZED (V) AND HORIZONTALLY POLARIZED (H) RECEIVE CHANNELS

Channel Name & Pol.	Center Freq. (GHz)	Band-width (MHz)	Footprint Size (km)	Integration Period (ms)	Sample Interval (ms)	Channel ΔT^* (K)
19H	19.35	125	43 × 69	7.95	8.44	0.42
19V	19.35	125	43 × 69	7.95	8.44	0.45
22V	22.23	300	40 × 60	7.95	8.44	0.74
37H	37	750	28 × 37	7.95	8.44	0.38
37V	37	750	29 × 37	7.95	8.44	0.37
85H	85.5	2000	13 × 15	3.89	4.22	0.73
85V	85.5	2000	13 × 15	3.89	4.22	0.69

* Estimated instrument noise for SSM/I F08. Varies between sensors.

Previous investigators [4], [40] have used BG to optimally degrade the resolution of high-frequency channels to "match" that of lower frequency channels. Rather than do this, we optimize the resolution of each channel independently to fixed-size grids.

In most previous applications of BG to spatial measurement interpolation of radiometer data, the measurement layout and MRF were limited to small local areas and fixed geometries to reduce computation and enable precomputation of the coefficients [16], [17], [40]. Azimuthally averaged antenna gain patterns have also been used [35]. Other investigators [36] processed the measurements on a swath-based grid. The fixed geometry yields only a relatively small number of possible matrices, enabling computational saving by precomputation of the matrices. Unfortunately, the Earth-based grids used in the CETB produce a much more variable geometry than the fixed swath-based geometries, making this approach less viable since similar shortcuts cannot be used.

For BG processing considered here, we follow [19] to define "nearby" as regions where the MRF is within 9 dB of the peak response. Outside this region, the MRF is treated as zero. We compute the solution separately for each output pixel using the particular measurement geometry antenna pattern at the swath location and Earth azimuth scan angle. This increases the computational load but results in the best quality images. The value of γ is subjectively selected for each channel but is held constant for each of the rows in Table I.

We have found that the BG method occasionally produces artifacts due to poor condition numbers of the matrices that are inverted. To eliminate these artifacts, a median-threshold filter is used to examine a 3 × 3 pixel window area around each pixel. "Spikes" larger than 5 K above the local median are replaced with the median value within the window. Smaller variations are not altered.

E. SSM/I

The gridding and reconstruction methods can be applied to a variety of radiometers such as SMMR, SSM/I, SSMIS, AMSR-E, and WindSat. However, to illustrate the methods and their tradeoff, in this paper, we concentrate on describing the methods as applied to a particular sensor, i.e., the SSM/I. We briefly describe this sensor here. The same techniques can be applied to the other sensors.
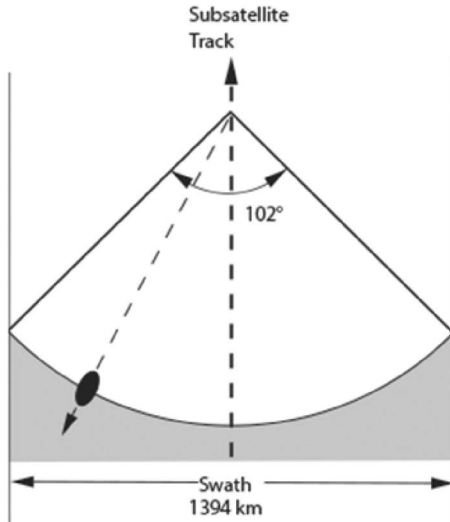
Fig. 3. Illustration of the SSM/I swath. The antenna and feed are spun about the vertical axis. Only part of the rotation is used for measuring brightness temperature: The rest is used for calibration. The incidence angle is essentially constant as the antenna scans the surface. This diagram is for the aft-looking F08 SSM/I. Later, SSM/Is looked forward but had the same swath width.
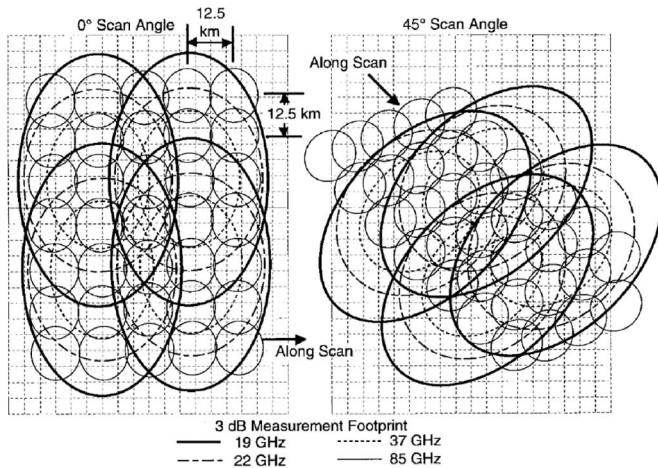

Fig. 4. Illustration of the individual 3 dB footprints of the various channels shown at two different antenna rotation angles. Only footprints for the vertically polarized channels are shown. Note the change in orientation (rotation) of the footprints with respect to the underlying Earth-fixed grid reference [19].

The SSM/I is a total-power radiometer with seven operating channels (see Table I). An integrate-and-dump filter is used to make radiometric brightness temperature measurements as the antenna scans the ground track via antenna rotation [37]. First launched in 1987, SSM/I instruments and their follow-ons, i.e., SSMIS, have flown on multiple spacecraft continuously until the present as part of the Defense Meteorological Satellite Program (DMSP) (F) satellite series.

The SSM/I swath and scanning concept is shown in Fig. 3. The antenna spin rate is 31.6 r/min with an along-track spacing of approximately 25 km. Multiple horns at 85 GHz provide along-track spacing for these channels at 12.5 km. The brightness temperature measurements are collected at a nominal incidence angle of approximately 53°. A zoomed view of the arrangement of the antenna footprints on the surface for different antenna azimuth angles is shown in Fig. 4.

V. RECONSTRUCTION PERFORMANCE SIMULATION

To compare the performance of the reconstruction techniques, it is helpful to use simulation. The results of these simulations inform the tradeoffs needed to select processing algorithm parameters. A simple (but realistic) simulation of the SSM/I geometry and spatial response function is used to generate simulated measurements of a synthetic Earth-centered image. From both noisy and noise-free measurements, non-enhanced (GRD), AVE, SIR, and BG images are created, with error (mean and rms) determined for each case. This is repeated separately for each channel. The measurements are assumed to have a standard deviation of $\Delta T = 1$ K. The results are relatively insensitive to the value chosen.

Two different pass cases are considered: the single-pass case and the case with two overlapping passes. Simulation shows that the relative performance of SIR and BG are the same for both cases; therefore, we show only one case in this paper. Since multiple passes are often combined in creating CETB images, the two-pass case is emphasized in the simulations presented. First, the size of the pixels for each channel must be determined. To generate images that can be embedded, the product pixel size is restricted to fractional power of two of 25 km. That is, the pixel size P_s in kilometers is given by

$$P_s = \frac{25}{2^{N_s}} \qquad (19)$$

where N_s is the pixel size scale factor, which is limited to the values 0, 1, 2, 3, and 4. The set of potential values of P_s are thus 25, 12.5, 6.25, 3.125, and 1.5625 km. For the simulation, the equal-area pixels are square.

An arbitrary "truth" image is generated with representative features, including spots of varying sizes, edges, and areas of constant and gradient T_B (see Fig. 5). The precise algorithm optimums can depend on the truth image used [20]. However, the other images considered in this paper produced similar results; therefore, for clarity, the results from only a single truth image are presented in this paper.

Based on the SSM/I measurement geometry, simulated locations of antenna boresite at the center of the integration period are plotted for a particular channel (37 GHz) in Fig. 6(a) for a single pass. Images calculated in the polar regions can combine measurements from multiple passes of the spacecraft over the same area. While the sampling for a single pass is fairly regular, the sampling from multiple overlapping passes tends to be less regular. Fig. 6(b) illustrates the sampling resulting from two overlapping passes. The variation in sample locations with each 25-km grid element is apparent.

The MRF is modeled with a 2-D Gaussian function whose 3 dB (half-power) point matches the footprint sizes given in Table I. The orientation of the ellipse varies over the swath according to the azimuth antenna angle. To apply the MRF in the processing, the MRF is positioned at the center of the nearest neighbor pixel to the measurement location and oriented with the azimuth antenna angle. The values of the discrete MRF are computed at the center of each pixel in a box surrounding the pixel center. The size of the box is defined to be the smallest enclosing box for which the sampled antenna pattern is larger
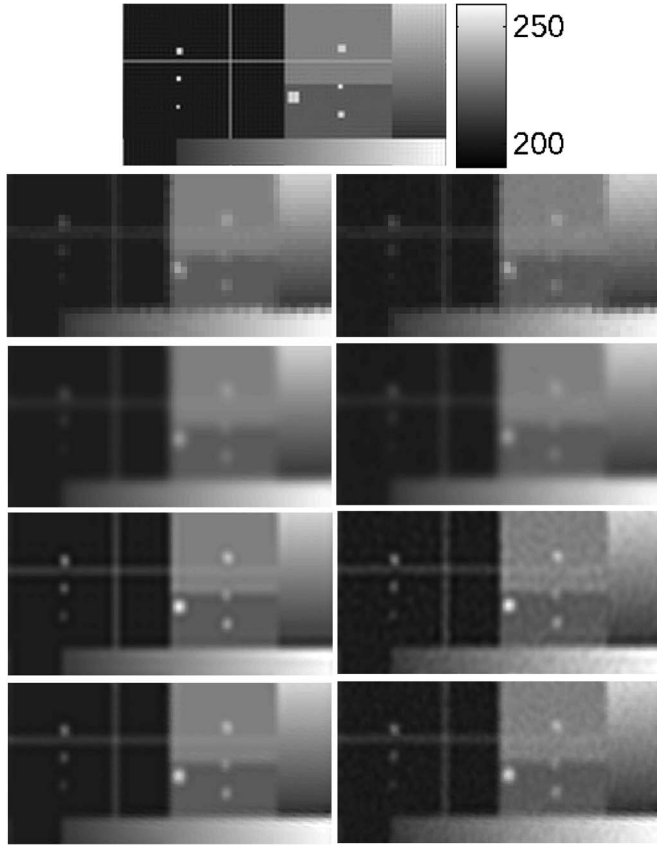
Fig. 5. SSM/I 37-GHz simulation results in Kelvin. (Top Panel) The "true" brightness temperature image. (Left Column) Noise-free simulation results. (Right column) Noisy simulation results). (Top row) 25 km GRD. (Second row) AVE. (third row) SIR (20 iterations). (Bottom row) BG with $\gamma = 0.85\pi$. Error statistics are summarized in Table II.
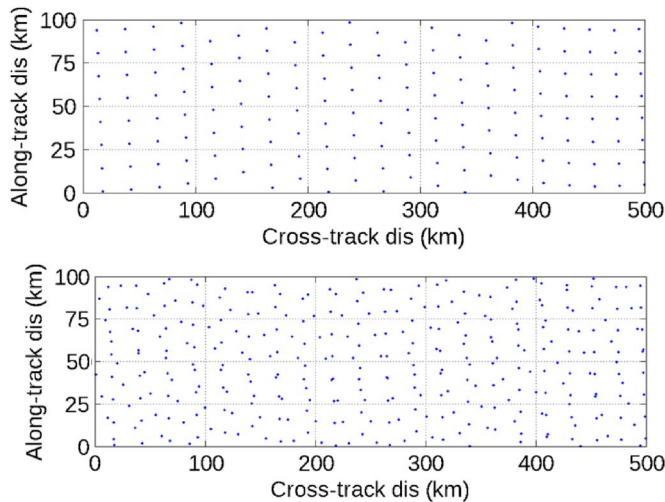

Fig. 6. Illustrations of the measurement locations within a small area of the SSM/I coverage swath. (Top) Locations for a single orbit pass. (Bottom) Locations for two passes.

than a minimum gain threshold of -30 dB relative to the peak gain. A second threshold (typically -9 dB) defines the gain cutoff used in the SIR and BG processing. The latter threshold defines the N_{size} parameter used in [19].

The image pixel size defines how well the MRF can be represented in the reconstruction processing and the simulation. Since we want to evaluate different pixel sizes in this simulation, a representative plot of the MRF sampling for each channel for each pixel size under consideration is shown in Fig. 7. Note that, as the pixel size is decreased, the sampled MRF more closely resembles the continuous MRF, thereby reducing quantization error; however, reducing the pixel size increases the computation and size of the output products.

GRD images are created by collecting and averaging all measurements whose center falls within each 25-km grid element. For comparison with high-resolution BG and SIR images in this paper, the GRD image is pixel-replicated to match the pixels of the SIR or BG images.

Separate images are created for both noisy and noise-free measurements. Error statistics (mean, standard deviation, and rms) are computed from the difference between the "truth" and estimated images for each algorithm option. The noise-only rms statistic is created by taking the square root of the difference of the squared noisy and noise-free rms values.

Both single and dual-pass cases were run as part of this paper, but only the dual-pass cases are shown in this paper. Fig. 5 shows a typical simulation result. It shows the true image, and both noise-free and noisy images. The error statistics for this case are given in Table II. For this pixel size, the image size is 448×224 with $P_s = 3.125$ km. In all cases, the error is effectively zero mean. The nonenhanced results have the larger errors, with the AVE results slightly less. The rmse is the smallest for the SIR results. Visually, GRD and AVE are similar, although SIR images better define edges. The spots are much more visible in the SIR images than in the GRD images, although the SIR image has a higher apparent noise "texture." BG results are discussed in a later section.

A. SIR Processing

Theoretically, SIR should be iterated to convergence to ensure full signal reconstruction. This can require hundreds of iterations [20]. However, continued SIR iteration also tends to amplify the noise in the measurements. By truncating the iteration, we can tradeoff signal reconstruction accuracy and noise enhancement. Truncated iteration results in the signal being incompletely reconstructed (partial reconstruction) with less noise. The reconstruction error declines with further iteration as the noise increases.

To understand the tradeoff between number of iterations and signal and noise, Fig. 8 shows noisy and noise-free SIR images for several different iteration numbers (recall that AVE is the first iteration of SIR). Note that as the number of iterations is increased, the edges are sharpened and the spots become more evident. Fig. 9 plots the mean, standard deviation, and rms versus iteration. Moreover, shown in this figure are the errors for the GRD and AVE (the first iteration of SIR) images. The noise texture grows with increasing iteration. We thus conclude that although iteration improves the signal, extended iteration can overenhance the noise.

Plotting the signal reconstruction error versus noise power enhancement as a function of iteration number in Fig. 9 can
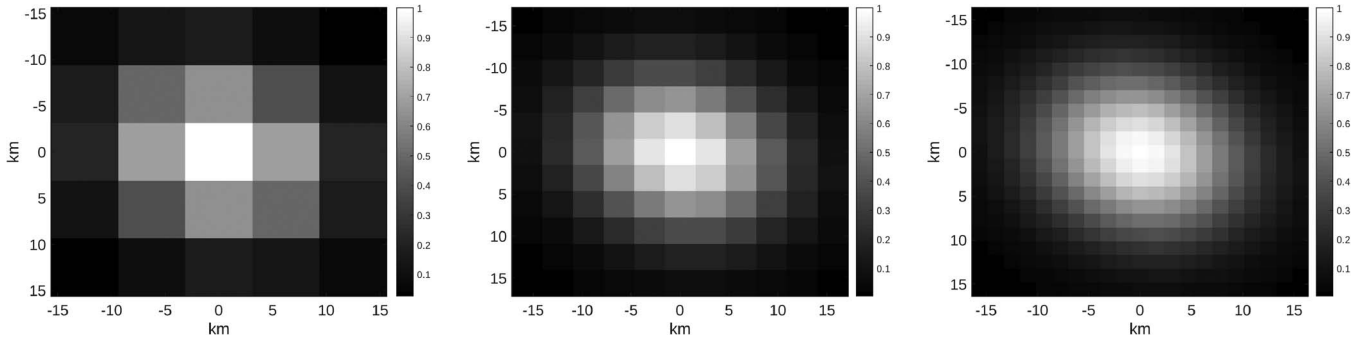
Fig. 7. Sampled MRF for different pixel sizes for an 85-GHz SSM/I channel. (Left) 6.25-km pixels. (Center) 3.125-km pixels. (Right) 1.5625-km pixels.

TABLE II
ERROR STATISTICS FOR TWO-PASS SIMULATION FOR 37 GHz,
$P_s = 3.125$ km. SIR USES 20 ITERATIONS. BG USES $\gamma = 0.85\pi$

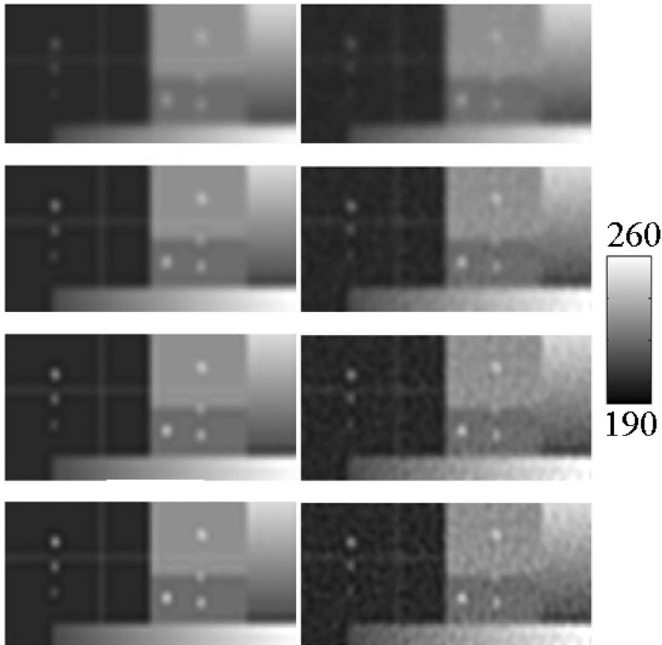| Case	Mean	STD	RMS
N-F GRD	0.00	3.96	3.96
N-F AVE	0.00	3.94	3.94
N-F SIR	0.00	3.33	3.33
N-F BG	0.00	3.52	3.52
Noisy GRD	0.01	4.08	4.08
Noisy AVE	0.00	3.97	3.97
Noisy SIR	0.01	3.55	3.55
Noisy BG	0.01	5.58	5.58

Fig. 8. SIR-reconstructed images for different iteration numbers in Kelvin. (Left column) Noise-free simulation results. (Right column) Noisy simulation results. (Rows, top to bottom) 1 iteration (AVE), 10 iterations, 20 iterations, and 30 iterations.
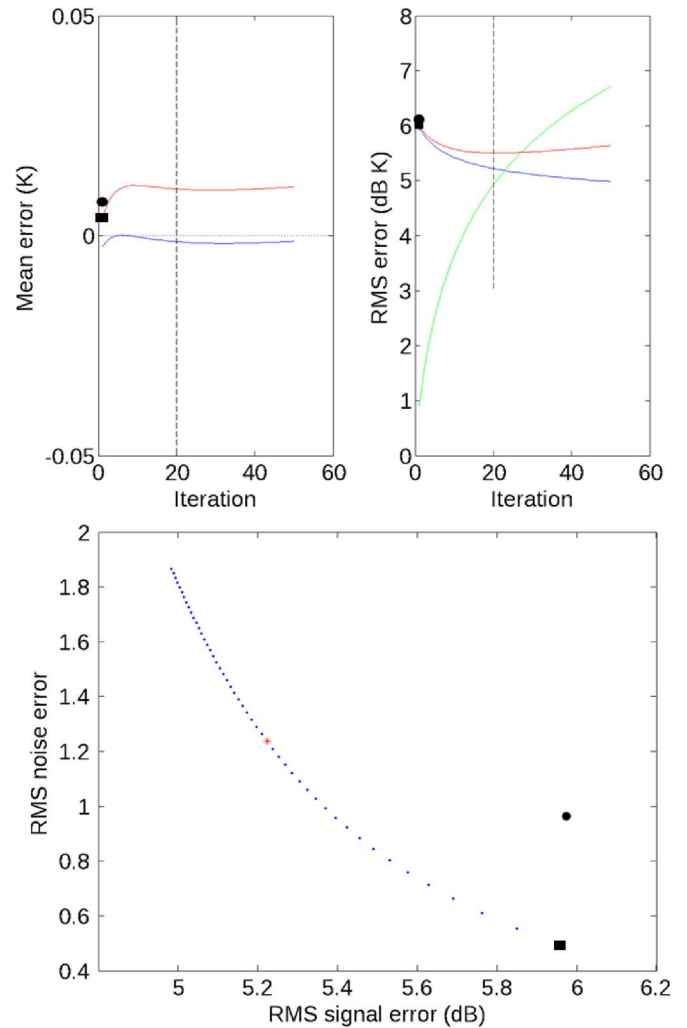
Fig. 9. (Top) SIR reconstruction error versus iteration number. (Upper left) mean error. (Upper right) rmse. The red line is the noisy measurement case, whereas the blue line is the noise-free measurement case. Green is the noise power computed from the difference between the noisy and noise-free cases. The green line is vertically displaced for clarity. The large spot is the error for the GRD image, whereas the large square is for AVE. The "optimum" (minimum error) number of iterations occurs at the minimum of the red curve. For reference, the dashed vertical line is shown at 20 iterations. (Bottom) RMS noise power versus rms signal error for each iteration, which extends from right to left. The large spot denotes the GRD result, whereas the large square is the AVE result. The star is SIR at 20 iterations.

help make a choice for the number of iterations that balances signal and noise performance. Note that the GRD result is much noisier and that the signal error improves with each iteration of SIR. Noting that we can stop the SIR iteration at any point, we somewhat arbitrarily choose a value of 20 iterations, which provides good signal performance and only slightly degraded

noise performance. This is the value used in Table II, where we see that the overall error performance of the SIR reconstruction is better than the GRD result.

TABLE III
TOTAL RMSE FOR NOISY TWO-PASS SIMULATION USING
$N_s = 3$ ($P_s = 3.125$) AND 20 SIR ITERATIONS

Case	GRD (K)	AVE (K)	SIR (K)
19 GHz	4.60	4.76	4.10
37 GHz	4.09	3.97	3.55
85 GHz	3.72	2.97	3.01

This analysis is repeated for different values of N_s, i.e., the number of passes, and for each radiometer channel. While the numerical values of the rmse change, the overall ranking and relative spacing of the GRD and SIR values are the same for all cases. Based on these detailed results (not shown), the following observations can be made.

1) With proper choice of the number of iterations SIR always has better signal performance (as well as better spatial resolution) than GRD.
2) Iterating SIR too long causes it to have worse noise performance than GRD, although the signal performance improves for longer iterations.
3) Based on the rmse comparison, SIR performance is slightly better than BG with the optimum γ.

In general, we want to use a small N_s to minimize computation and to minimize the number of iterations. Based on Nyquist criteria for sampling the response pattern, $N_s = 2$ is the minimum usable value. With the idea that we want to keep the same values for all channels, if possible, for consistency, it appears that $N_s = 3$ (i.e., $P_s = 3.125$ km) provides the best overall performance for all channels and that 5–20 iterations provide a reasonable tradeoff between signal and noise. Using $N_s = 3$, Table III provides a performance comparison for the rmses of GRD, AVE, and SIR for the different channels using 20 iterations. Fig. 5 compares the resulting noisy simulation results. Note that, although the pixel size is 3.125 km, the effective spatial resolution of the images is, of course, coarser than this. Recall that at least some of the extra pixel resolution is required to properly process the signal to meet the Nyquist signal representation requirements and represent the higher frequency content of the high-resolution images. It should be noted that the precise minimum value depends on the exact noise realization; however, the optimum can only be computed in simulation; therefore, we have chosen the nominal optimum and use it for the processing of real data.

In summary, SIR provides better spatial resolution and lower overall rmse than conventionally gridded (GRD) products. The reconstruction does tend to enhance the noise, but this is offset by reduced signal error. The total error can be controlled by the number of iterations to tradeoff noise and resolution.

B. BG Processing

The BG approach requires selection of a subjective tuning parameter. It also requires significantly more computation than does SIR. Previous investigators who worked on swath-based grids were able to coarsely quantize the possible measurement positions to reduce the number of matrix inversions required. This enabled them to generate precomputed approximate solutions [18], [40]. However, as noted previously, the situation is different when working with Earth-based grids. Note that, Fig. 4, the measurement centers are irregularly arranged with respect to the Earth-located pixel grid. This limits any ability for using similar preprocessing techniques to speed the BG computation. Further, to avoid the approximations used with fixed geometries, we use the actual measurement positions and a general pixel grid so that reconstruction can be done on the Earth-located pixel grid [19]. Another advantage of this approach is that all data from overlapping swaths (subject to ltod) can be used, whereas previous implementations used data from one swath for any given Earth grid cell [16], [17]. The general form we use requires creating and inverting a matrix for each image pixel.

In the BG simulations in the following, the same simulated SSM/I measurements are used as in the SIR simulations. In [19], note that SIR and BG results appear similar, but SIR has slightly better performance in simulation and is much faster than BG. Our simulations for SSM/I confirm this conclusion. As noted, the BG γ controls the regularization and relative weighting between signal reconstruction and noise enhancement. The value of γ can range from 0 to $\pi/2$. Note that, for simplicity in the captions and plots, the symbols γ' or g are sometimes used, which are related to γ by $\gamma = (\pi/2)\gamma'$ and $\gamma = \pi g$.

A BG image for a particular γ closely resembles a SIR image for a particular iteration number. For small values of γ', the noise is the most enhanced but the features are sharpest. For larger values of γ', the noise texturing is reduced but features are smoothed. A plot of the rmse versus γ' is shown in Fig. 10. Note that noise-free and noisy results are shown both for BG and BG after median filtering. Due to a poorly conditioned matrix, some BG-estimated pixels have extreme values. These can be suppressed by applying a 3×3 median filter after the BG processing. The median filter can significantly reduce the rms noise and artifacts in the image without significantly degrading the image quality. The median filter is edge preserving and so has minimal effect on the image quality.

Similar to the analysis of number of iterations for SIR, it is useful to compute the noise and signal rmse, which varies with the value of γ'. An example for the 37-GHz channel with $N_s = 3$ is shown in Fig. 10. A numerical comparison of the results is shown in Table II. BG for the optimum γ is noisier than SIR with the optimum number of iterations.

Other examples of BG images versus different gamma parameters were considered. Large values of N_s result in excessive (and impractical) run times. Fortunately, the rmse varies only slightly with changes in N_s and the same value selected for SIR processing can be used. All cases have a minimum total rmse near $g = 0.85$; therefore, for consistency, we adopt this value, i.e., $\gamma = 0.85\pi$, for all channels and all values of N_s.

We find that BG requires at least an order of magnitude more computation time than SIR. For larger values of N_s, it requires several orders of magnitude more computation time; hence, the desire for small values of N_s. The choice of γ does not affect the computation, but changing the antenna gain cutoff from -9 dB to larger values can reduce the number of local measurements
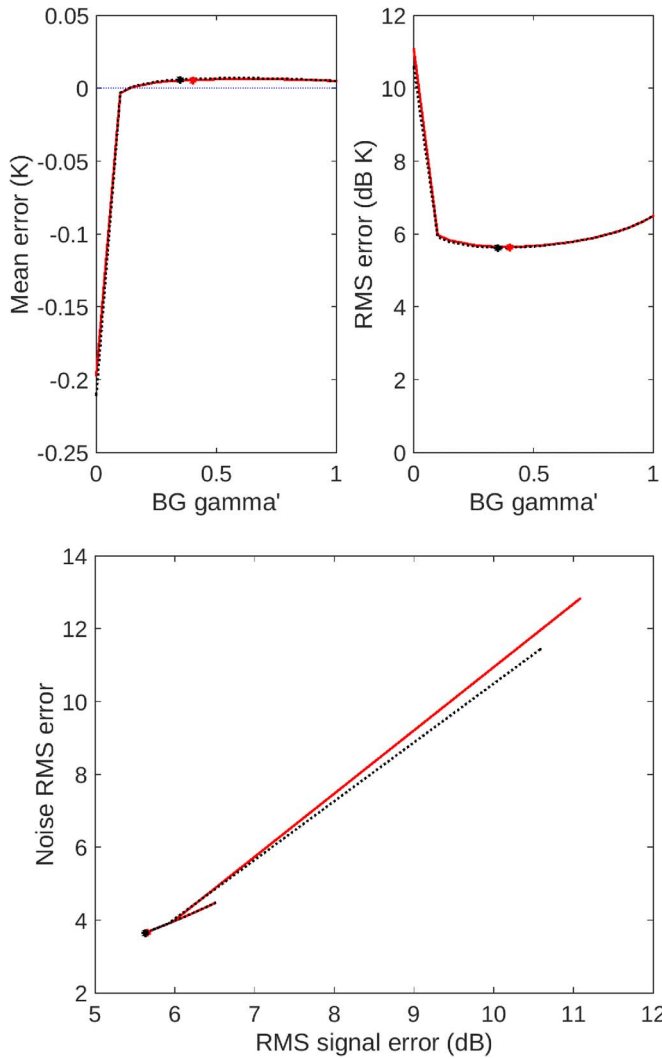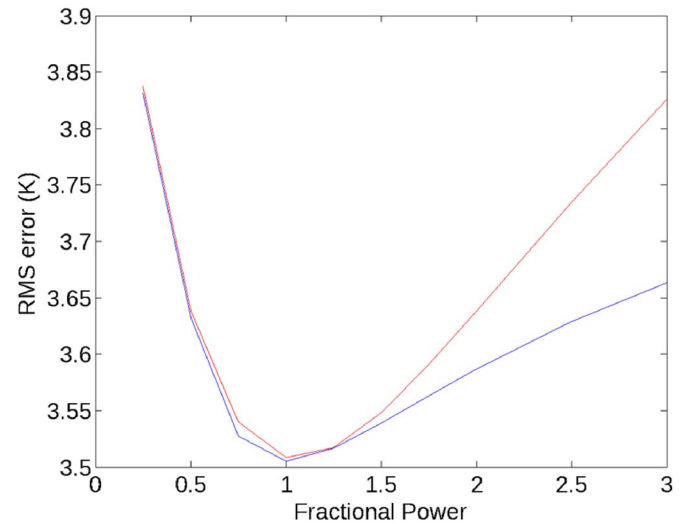
Fig. 11. Plots of the noisy total rmse resulting from simulating measurements with the MRF and using an erroneous MRF from (20) versus fractional power ρ. The dotted curve is the SIR error at 20 iterations. The solid curve shows the rmse resulting from minimizing the total rmse versus SIR iteration number.

Fig. 10. (Top) BG error versus versus γ'. (upper left) mean error. (Upper right) rmse. The location of the optimum (i.e., the minimum rmse) values is indicated with asterisks. (Bottom) RMS noise versus RMS signal error for different γ'. The solid line is noisy BG, whereas the dotted line is after thresholded median filtering. These lines often coincide in the plots.

included in the matrix inversion and thus the required CPU time. Changing the gain threshold is not considered here.

In summary, BG and SIR provide similar results, and both provide better spatial resolution and overall rmse than conventionally gridded (GRD) products. BG is, however, computationally demanding. Final selection of BG versus SIR for CETB will rely on input from the user community.

VI. RECONSTRUCTION SENSITIVITY TO INACCURACY IN THE DESCRIPTION OF THE MRF

As previously noted, the MRF for some sensors is not known very well. Even for those for which the MRF is known, there are uncertainties (errors) in the description of the MRF. This leads to the following question: How sensitive is the reconstruction to the accuracy of the MRF? In pursuing this question, we consider only the SIR algorithm in this paper. However, we find similar performance using BG. We note that we are interested

in the partial reconstruction case when only a relatively small (5–20) number of SIR iterations is performed.

To address the question of reconstruction sensitivity, an experimental study is conducted in which simulated measurements of a synthetic scene are generated using the full MRF previously described. Then, different (erroneous) MRF descriptions are used in the reconstruction process. The results from the correct description and the erroneous descriptions are then compared.

Although other erroneous MRFs were considered in a larger study [10], in this paper, we consider the family of erroneous MRFs defined to be a power of the true MRF. That is, the MRF used for reconstruction $R'(x, y)$ is computed from the true MRF $R(x, y)$ using

$$R'(x, y) = R^\rho(x, y) \tag{20}$$

where $0 < \rho < 3$. As ρ is varied in the range of 0.25–3, the area of the 3-dB footprint changes, and the response pattern rolloff characteristics change. Fig. 11 plots the total noisy rmse versus ρ for this case. Two curves are shown. One is for a fixed number of iterations (20 in this case), and the other is the rmse resulting when selecting the number of SIR iterations that minimize the total rmse. This is the optimum number of SIR iterations. Note that, in all cases, the variation in the rmse is small, and the difference between the fixed and the optimum number of iterations is also very small.

These simulation results reveal that using the correct MRF for reconstruction minimizes the error, but modest distortions in the MRF used in the reconstruction have a limited impact on the accuracy of the reconstruction results. The variation in total rmse with MRF distortion is small for all channels and cases. Thus, the results of the reconstruction are not particularly sensitive to the accuracy of the MRF, and we can successfully use approximate MRF models. This is a fortunate result because it

means that precise antenna pattern descriptions are not required in computing MRF.

To explain this result, consider that since the noise is amplified as the signal is enhanced, there is a tradeoff between the signal reconstruction error and the noise increase. This tradeoff leads us to truncate the iterative reconstruction process before it is complete, i.e., the result is only a partial reconstruction. The simulations show that the partial reconstruction can tolerate modest errors in the MRF description and still yield reasonable estimates of the desired signal. Not shown is that when the erroneous MRF is used to attempt to fully reconstruct the signal, the final signal can be significantly distorted compared to the signal resulting from the correct MRF description.

VII. ACTUAL DATA

While the previous results are based on simulation, here, we compare GRD and enhanced-resolution products using actual data (see Fig. 12). These evening ltod images are small (250 km × 250 km) subimages extracted from the full EASE-Grid-2.0 Northern Hemisphere grid for day 61 of 1997 using the selected grid size and algorithm parameters derived from simulation. A visual comparison of the images reveals improved detail in the SIR and BG images compared with the GRD images. Note that, when using actual data, the true T_B values are not known; therefore, errors cannot be computed.

As expected, the GRD images are blocky, whereas the high-resolution images exhibit finer resolution. Subjectively, the SIR images have the highest contrast and appear more detailed than the BG images, but there is also somewhat more noise in the SIR images compared with the BG images. Note that the effective resolution varies between channels, with the highest frequency channels (which have the smallest MRFs) providing the finest resolution. The differences in T_B with polarization show that vertically polarized images appear in general brighter than horizontally polarized images. Further interpretation of the T_B images is left to other papers.

VIII. CONCLUSION

The NASA-sponsored Calibrated Passive Microwave Daily EASE-Grid 2.0 Brightness Temperature ESDR (CETB) project is producing a multisensor multidecadal time series of gridded radiometer products from consistently calibrated T_B measurements from SMMR, SSM/I, SSMIS, and AMSR-E. The CETB product includes both conventional 25-km gridded images and high-resolution radiometer products designed to support climate studies. This paper has considered two primary high-resolution image reconstruction algorithms: the BG approach and the radiometer form of SIR algorithm. In effect, for each pixel, BG inverts a local matrix that describes the interaction of measurements near the pixel of interest and a different matrix that depends on the relative location and spatial measurement response pattern of the measurements. This matrix is regularized by including the noise covariance. The iterative SIR algorithm reconstructs the image from the measurements using the measurement locations and response patterns. SIR is equivalent to inverting the full matrix reconstruction matrix for the entire
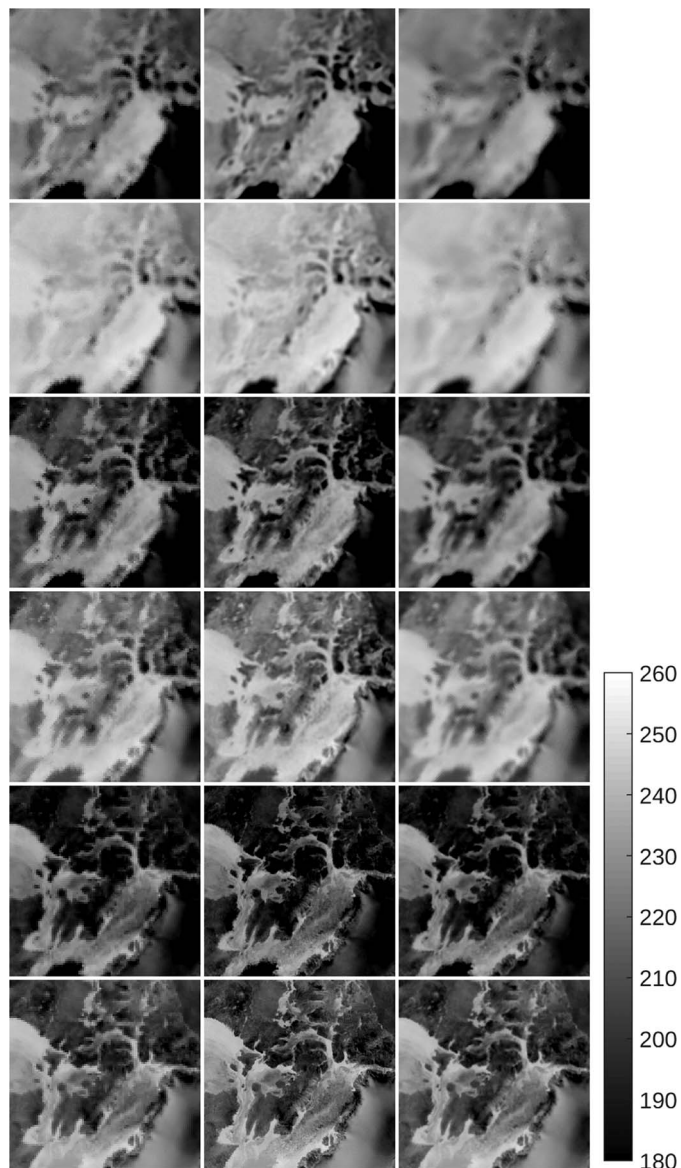

Fig. 12. Subimages extracted from a one-day CETB Northern Hemisphere SSM/I EASE-Grid 2.0 image product: (left column) GRD, (Center Column) SIR, and (Right Column) BG, and (each row, top to bottom) for channels 19H, 19V, 37H, 37V, 85H, and 85V. The area shown spans 250 km × 250 km and is centered over Baffin Island west of Greenland, which is partially visible in the lower right corner. No-data pixels in the GRD images have been filled with the median of nearby pixels units in Kelvin.

image but is regularized by truncating the iteration, resulting in only partial reconstruction. Both SIR and BG provide higher spatial resolution surface brightness temperature images with smaller total error compared with conventional DIB gridded image formation.

A tradeoff study is summarized for selecting optimum grid resolution, the number of SIR iterations, and the BG gamma parameter. Although the optimum values vary somewhat between sensors and sensor channels, we constrain the selected parameters to a common set of values. We found that although both image formation approaches are effective in improving the spatial resolution of the surface brightness temperature estimates, SIR however requires less computation. Our analysis

TABLE IV
GRIDS AND RECONSTRUCTION PARAMETERS PLANNED FOR CETB SENSORS AND CHANNELS.
NOT ALL CHANNELS ON EACH SENSOR ARE PROCESSED. GRIDS ARE NESTED TO OVERLAY

Sensor name	Channels used	GRD pixel size (km)	Pixel size scale factor (N_s) and size (km)	SIR iterations	BG $g = \gamma/\pi$
SMMR	6.6H, 6.6V	25	(1) 12.50	20	0.85
	10.7H, 10.7V, 18H, 18V, 21H, 21V, 37H, 37V	25	(2) 6.250	20	0.85
SSM/I	19H, 19V, 22V, 37H, 37V,	25	(2) 6.250	20	0.85
	85H, 85V	25	(3) 3.125	20	0.85
SSMIS	19H, 19V, 22V, 37H, 37V	25	(3) 3.125	20	0.85
	91H, 91V	25	(3) 3.125	20	0.85
AMSR-E	6.9H, 6.9V	25	(2) 6.250	20	0.85
	10.7H, 10.7V, 18,7H, 18.7V, 23.8H, 23.8, 36.5H, 36.5V	25	(2) 6.250	20	0.85
	89H, 89V	25	(3) 3.125	20	0.85

of the sensitivity of the reconstruction to the accuracy of the MRF shows that the partial reconstruction selected based on the noise tradeoff can tolerate errors in the description of the sensor measurement response function. This simplifies the processing of sensor data for which the measurement response function is not known.

A summary of the reconstruction parameters selected for the CETB project for each sensor channel is summarized in Table IV.

APPENDIX

Here, we consider the spatial frequency information within an SSM/I measurement by computing the wavenumber spectrum of the MRF. Fig. 13 provides a conceptual illustration of the projection of the sensor antenna pattern on the Earth's surface in the elevation plane and the geometry definitions used in the following. From the geometry and temporarily assuming a spherical Earth, the nominal slant range R between the sensor and boresite location can be computed from the spacecraft height H, the incidence angle θ_i, and the (local) radius of the Earth R_e using

$$R = \frac{R_e}{\sin(180 - \theta_i)} \sin\left[\theta_i - \sin^{-1}\frac{R_e \sin(180 - \theta_i)}{(R_e + H)}\right]. \quad (21)$$

Aligning the x coordinate with the look direction at azimuth angle $\phi = 0$, on a locally tangent plane, the approximate x displacement is $dx \approx R d\theta_i / \sin\theta_i$. Since the incidence angle for the SSM/I is approximately 53°, $1/\sin\theta_i \approx 1.252$; therefore, the nominally circular antenna pattern is elongated on the surface in the range direction by about 25%, resulting in an elliptical footprint on the surface. As previously noted, the instantaneous antenna pattern is smeared in the rotation (azimuth) direction by the temporal signal averaging.

Given the elevation angle and height, for a particular displacement Δx along the Earth's surface from the intersection of the antenna boresite vector at elevation angle, the antenna elevation angle offset $\Delta\xi$ is computed by first determining the Earth angle α_0 (see Fig. 13) using

$$\xi = \sin^{-1}\left[\frac{R_e}{(R_e + H)}\sin(180 - \theta_i)\right] \quad (22)$$

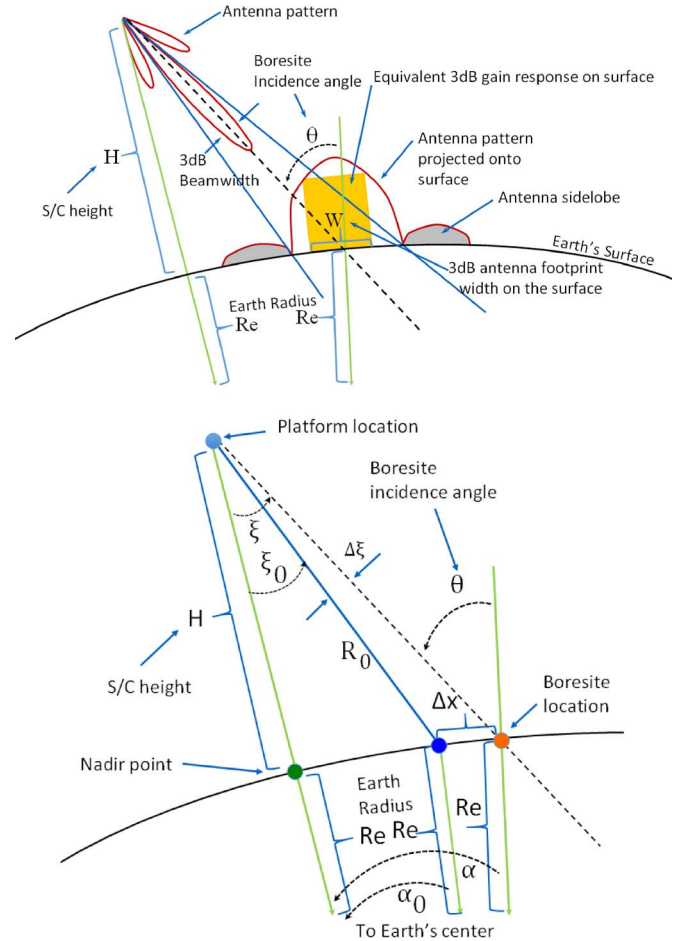$$\alpha_0 = \theta_i - \xi - \Delta x/R_e. \quad (23)$$

Fig. 13. (Top) Conceptual diagram illustrating the projection of the instantaneous radiometer antenna pattern on the Earth's surface. (Bottom) Geometry for computation.

The antenna elevation offset angle corresponding to the point of interest at Δx is computed as

$$R_0 = \sqrt{(R_e + H)^2 + R_e^2 - 2(R_e + H)R_e \cos\alpha_0} \quad (24)$$

$$\Delta\xi = \xi - \sin^{-1}\left[\frac{R_e}{R_0}\sin\alpha_0\right]. \quad (25)$$

These equations provide a formula to relate surface displacement from the boresite to the change in the elevation angle.

It is known that the far-field antenna pattern can be expressed as the Fourier transform of the electric field across the effective aperture of the antenna [25]. Since the effective aperture is, by definition, finite extent, this implies that the antenna pattern is angularly bandlimited. This argument has been used to suggest that the wavenumber spectrum (the 2-D spatial Fourier transform) of the MRF is similarly bandlimited. However, it should be noted that the aperture-to-far-field Fourier transform is computed in angular units, whereas the spectrum of the MRF is in km^{-1} on the surface. As derived earlier, there is a nonlinear transformation between angle and surface distance. Further, the angular Fourier transform is periodic in angle, whereas the surface spectrum Fourier is computed over a finite domain and is therefore infinite in extent. In the following, we consider these issues in more detail and compute the approximate spectrum of the MRF.

As previously described, the MRF results from projecting the antenna pattern onto the surface and integrating the moving pattern over the integration period. The projection stretches and compresses the pattern on the Earth's surface. Due to the curvature of the Earth, not all of the antenna pattern is projected onto the Earth's surface. Thus, the MRF contains only part of the antenna pattern, i.e., the pattern is clipped. This can be modeled as the multiplication of the stretched antenna pattern by a rectangular window or boxcar function. The inverse R term in the spherical propagation factor has the effect of tapering the projection of the antenna gain onto the surface MRF. For simplicity, this factor is ignored in the following discussion. Integration has only a small effect on the projected elevation gain.

As evident from (22)–(25), the projection in elevation is nonlinear. The MRF on the surface is a nonlinearly stretched and windowed (clipped) version of the original antenna pattern. In principle, the wavenumber (spatial) spectrum of the MRF can be analytically derived from the projecting and clipping functions. However, this is quite complicated, and we resort to numerical methods. Recall from signal processing theory that the Fourier transform of the product of two functions is the convolution of the Fourier transforms of the individual functions. In this case, the convolution yields a wider region of support in frequency domain than either of the individual functions. Furthermore, since the clipping window function is finite length, its Fourier transform is infinite in extent (though it can have nulls). The convolution of an infinite-extent function with any function results in an infinite-extent function. It thus becomes apparent that the region of support of the MRF is not bounded, i.e., at the surface, the MRF is not truly bandlimited, although the aperture illumination pattern is.

The wavenumber (spatial frequency) of the MRF informs us about the information content in the radiometer measurements. The nonlinearity in the projection from antenna pattern to the MRF produces a broader region of support for MRF wavenumber spectrum than suggested from the finite region of support of the antenna pattern illumination function, although there is attenuation of the high-wavenumber portions of the spectrum and portions of the high-wavenumber spectrum are unrecoverable due to low gain.

The top two panels of Fig. 14 illustrate a slice through the idealized 19-GHz SSM/I pattern over the full angular extent of
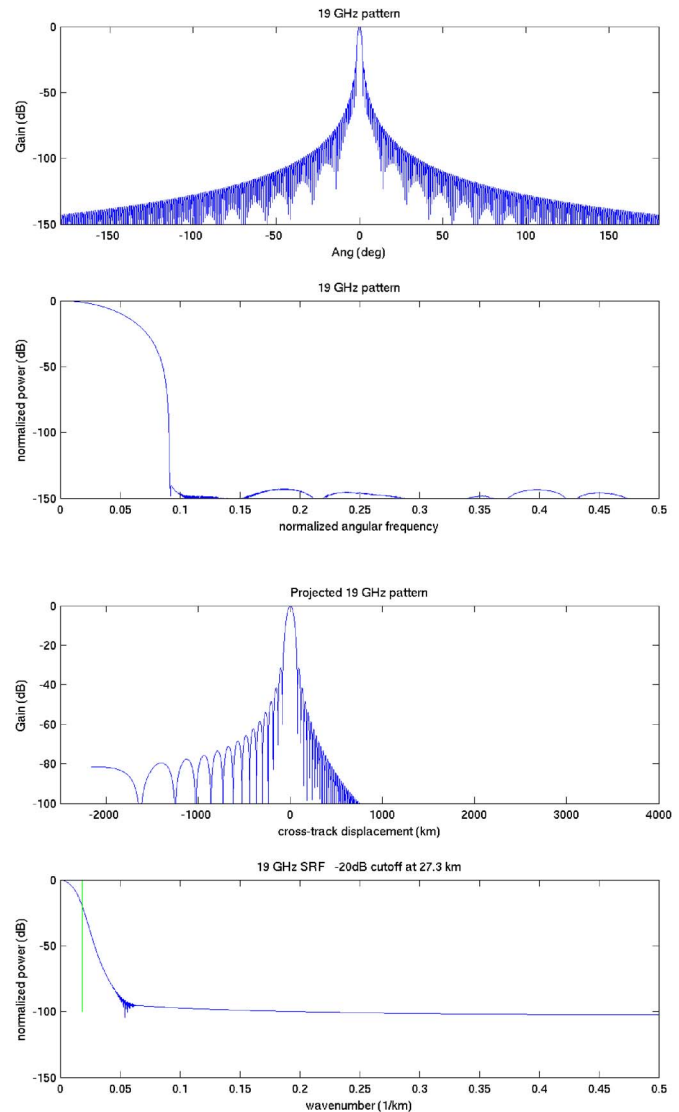

Fig. 14. (Top panel) Magnitude squared plot of elevation slice through an idealized 19-GHz SSM/I channel antenna pattern. (Second panel) Magnitude Fourier transform. This is the magnitude of the aperture illumination function. (Third panel) Antenna pattern projected onto the Earth versus displacement along the surface. The x-axis is the range over which the platform is visible from the surface. Note the variable spacing of the sidelobes. (Bottom panel) Magnitude Fourier transform of the slice of the projected antenna pattern. The vertical line is at −20 dB and corresponds to a 27 km spatial scale. For comparison, the 3-dB scale corresponds to 43 km.

the pattern (the effects of spacecraft blockage are ignored), and the corresponding Fourier transform, which is $E_a(r_a)$, has a finite region of support as expected. The other channels have similar results, although for shorter wavelengths, the pattern is narrower and the frequency support is wider. Projecting the elevation-slice antenna pattern on to the Earth's surface using typical SSM/I measurement geometry results in the gain pattern on the Earth's surface, as shown in the bottom panels of Fig. 14. The wavenumber spectrum has units of inverse ground distance, with a scale distance that is twice the inverse of the wavenumber. The region of support in surface wavenumber has a tapered rolloff. As expected, broader region of support confirms that we can recover as least somewhat more spatial information than merely assuming the spatial scale is set by the 3 dB footprint.

REFERENCES

[1] NASA, Data Processing Levels. Accessed 24 Apr. 2014. [Online]. Available: http://science.nasa.gov/earth-science/earth-science-data/data-processing-levels-for-eosdis-data-products

[2] K. W. Knowles, E. J. Njoku, R. L. Armstrong, and M. J. Brodzik, *Nimbus-7 SMMR Pathfinder Daily EASE-Grid Brightness Temperatures.* Boulder, CO, USA: National Snow and Ice Data Center/Digital Media, 2000. [Online]. Available: http://nsidc.org/data/nsidc-0071

[3] K. W. Knowles, M. H. Savoie, R. L. Armstrong, and M. J. Brodzik, *AMSR-E/Aqua Daily EASE-Grid Brightness Temperatures.* Boulder, CO, USA: National Snow and Ice Data Center/Digital Media, 2006. [Online]. Available: http://nsidc.org/data/nsidc-0301

[4] R. Armstrong, K. Knowles, M. Brodzik, and M. A. Hardman, *DMSP SSM/I-SSMIS Pathfinder Daily EASE-Grid Brightness Temperatures*, Version 1. Boulder, CO, USA: NASA DAAC/National Snow and Ice Data Center, 1994. [Online]. Available: http://nsidc.org/data/nsidc-0032

[5] M. J. Brodzik and K. W. Knowles, EASE-Grid: A versatile set of equal-area projections and grids, in *Discrete Global Grids*, M. Goodchild, Ed. Santa Barbara, CA, USA: National Center for Geographic Information and Analysis, 2012. [Online]. Available: http://www.ncgia.ucsb.edu/globalgrids-book/ease_grid/

[6] M. J. Brodzik, B. Billingsley, T. Haran, B. Raup, and M. H. Savoie, "EASE-Grid 2.0: Incremental but significant improvements for Earth-gridded data sets," *ISPRS Int. J. Geo-Inf.*, vol. 1, no. 1, pp. 32–45, Mar. 2012.

[7] M. J. Brodzik, B. Billingsley, T. Haran, B. Raup, and M. H. Savoie, "Correction: M. J. Brodzik, et al., EASE-Grid 2.0: Incremental but significant improvements for Earth-gridded data sets," *ISPRS Int. J. Geo-Inf.*, vol. 3, no. 3, pp. 1154–1156, Sep. 2014.

[8] F. J. Wentz, "SSM/I version-7 calibration report," Remote Sens. Syst., Santa Rosa, CA, USA, RSS Tech. Rep. 011012, 2013. [Online]. Available: http://images.remss.com/papers/rsstech/2012_011012_Wentz_Version-7_SSMI_Calibration.pdf

[9] H. Semunegus, W. Berg, J. J. Bates, K. R. Knapp, and C. Kummerow, "An extended and improved Special Sensor Microwave Imager (SSM/I) period of record," *J. Appl. Meteorol. Climatol.*, vol. 49, no. 3, pp. 424–436, Mar. 2010.

[10] M. J. Brodzik and D. G. Long, *Calibrated Passive Microwave Daily EASE-Grid 2.0 Brightness Temperature ESDR (CETB): Algorithm Theoretical Basis Document.* Boulder, CO, USA: National Snow and Ice Data Center (NSIDC), 2015. [Online]. Available: http://nsidc.org/pmesdr/files/2015/09/MEaSUREs_CETB_ATBD_v0.10.pdf

[11] J. Maslanik and J. Stroeve, *DMSP SSM/I-SSMIS Daily Polar Gridded Brightness Temperatures*, Version 4. Boulder, CO, USA: NASA DAAC/National Snow and Ice Data Center, 2004. [Online]. Available: http://nsidc.org/data/nsidc-0001

[12] G. E. Backus and J. F. Gilbert, "Numerical applications of a formalism for geophysical inverse problems," *Geophys. J. R. Astron. Soc.*, vol. 13, no. 1–3, pp. 247–276, Jul. 1967.

[13] G. E. Backus and J. F. Gilbert, "Resolving power of gross Earth data," *Geophys. J. R. Astron. Soc.*, vol. 16, no. 2, pp. 169–205, Oct. 1968.

[14] A. Stogryn, "Estimates of brightness temperatures from scanning radiometer data," *IEEE Trans. Antennas Propag.*, vol. AP-26, no. 5, pp. 720–726, Sep. 1978.

[15] G. A. Poe, "Optimum interpolation of imaging microwave radiometer data," *IEEE Trans. Geosci. Remote Sens.*, vol. 28, no. 5, pp. 800–810, Sep. 1990.

[16] J. F. Galantowicz and A. W. England, "The Michigan Earth grid: Description, registration method for SSM/I data, and derivative map projections," Radiation Lab., Dept. Elect. Eng. Comput. Sci., Univ. Michigan, Ann Arbor, MI, USA, Tech. Rep. 027396-2-T, 1991.

[17] J. F. Galantowicz, "Microwave radiometry of snow-covered grasslands for the estimation of land-atmosphere energy and moisture fluxes," Ph.D. dissertation, Dept. Elect. Eng. Comput. Sci./Dept. Atmos., Oceanic, Space Sci., Univ. Michigan, Ann Arbor, MI, USA, 1995.

[18] H. Gu and A. W. England, "AMSR-E data resampling with near-circular synthesized footprint shape and noise/resolution tradeoff study," *IEEE Trans. Geosci. Remote Sens.*, vol. 45, no. 10, pp. 3193–3203, Oct. 2007.

[19] D. G. Long and D. L. Daum, "Spatial resolution enhancement of SSM/I data," *IEEE Trans. Geosci. Remote Sens.*, vol. 36, no. 2, pp. 407–417, Mar. 1998.

[20] D. S. Early and D. G. Long, "Image reconstruction and enhanced resolution imaging from irregular samples," *IEEE Trans. Geosci. Remote Sens.*, vol. 39, no. 2, pp. 291–302, Feb. 2001.

[21] D. G. Long and J. Stroeve, *Enhanced-Resolution SSM/I and AMSR-E Daily Polar Brightness Temperatures.* Boulder, CO, USA: NASA DAAC/National Snow and Ice Data Center, Digital Media, 2011. [Online]. Available: http://nsidc.org/data/nsidc-0464

[22] B. A. Gunn and D. G. Long, "Spatial resolution enhancement of AMSR Tb images based on measurement local time of day," in *Proc. IEEE IGARSS*, Boston, MA, USA, Jul. 6–11, 2008, pp. V-33–V-36.

[23] T. Agnew, A. Lambe, and D. Long, "Estimating sea ice flux across the Canadian Arctic Archipelago using enhanced AMSR-E," *J. Geophys. Res.*, vol. 113, no. C10, Oct. 2008, Art. ID C10011.

[24] S. E. L. Howell, C. Derksen, and A. Tivy, "Development of a water clear of sea ice detection algorithm from enhanced SeaWinds/QuikSCAT and AMSR-E measurements," *Remote Sens. Environ.*, vol. 114, no. 11, pp. 2594–2609, Nov. 2010.

[25] F. Ulaby and D. G. Long, *Microwave Radar and Radiometric Remote Sensing.* Ann Arbor, MI, USA: Univ. of Michigan Press, 2014.

[26] F. Wentz, "Measurement of oceanic wind vector using satellite microwave radiometer," *IEEE Trans. Geosci. Remote Sens.*, vol. 30, no. 5, pp. 960–972, Sep. 1992.

[27] H. Stephen and D. G. Long, "Modeling microwave emissions of erg surfaces in the Sahara Desert," *IEEE Trans. Geosci. Remote Sens.*, vol. 43, no. 12, pp. 2822–2830, Dec. 2005.

[28] D. G. Long and M. R. Drinkwater, "Azimuth variation in microwave scatterometer and radiometer data Over Antarctica," *IEEE Trans. Geosci. Remote Sens.*, vol. 38, no. 4, pp. 1857–1870, Jul. 2000.

[29] H. Feichtinger and K. Gröchenig, "Iterative reconstruction of multivariate band-limited function from irregular sampling values," *SIAM J. Math. Anal.*, vol. 23, no. 1, pp. 244–261, 1992.

[30] K. Gröchenig, "Reconstruction algorithms in irregular sampling," *Math. Comput.*, vol. 59, no. 199, pp. 181–194, Jul. 1992.

[31] X. Xu, W. Ye, and A. Entezari, "Bandlimited reconstruction of multi-dimensional images from irregular samples," *IEEE Trans. Image Process.*, vol. 22, no. 10, pp. 3950–3960, Oct. 2013.

[32] D. G. Long and R. Franz, "Band-limited signal reconstruction from irregular samples with variable apertures," *IEEE Trans. Geosci. Remote Sens.*, vol. 54, no. 4, pp. 2424–2436, Apr. 2016.

[33] B. Caccin, C. Roberti, P. Russo, and A. Smaldone, "The Backus-Gilbert inversion method and the processing of sampled data," *IEEE Trans. Signal Process.*, vol. 40, no. 11, pp. 2823–2825, Nov. 1992.

[34] P. Chakraborty, A. Misra, T. Misra, and S. S. Rana, "Brightness temperature reconstruction using BGI," *IEEE Trans. Geosci. Remote Sens.*, vol. 46, no. 6, pp. 1768–1773, Jun. 2008.

[35] M. R. Farrar and E. A. Smith, "Spatial resolution enhancement of terrestrial features using deconvolved SSM/I brightness temperatures," *IEEE Trans. Geosci. Remote Sens.*, vol. 30, no. 2, pp. 349–355, Mar. 1992.

[36] P. J. Stephens and A. S. Jones, "A computationally efficient discrete Backus-Gilbert footprint-matching algorithm," *IEEE Trans. Geosci. Remote Sens.*, vol. 40, no. 8, pp. 1865–1878, Aug. 2002.

[37] J. P. Hollinger, J. L. Pierce, and G. A. Poe, "SSM/I instrument evaluation," *IEEE Trans. Geosci. Remote Sens.*, vol. 28, no. 5, pp. 781–790, Sep. 1990.

[38] F. Lenti, F. Nunziata, C. Estatico, and M. Migliaccio, "On the spatial resolution enhancement of microwave radiometer data in Banach spaces," *IEEE Trans. Geosci. Remote Sens.*, vol. 52, no. 3, pp. 1834–1842, Mar. 2014.

[39] F. Lenti, F. Nunziata, M. Migliaccio, and G. Rodriguez, "Two-dimensional TSVD to enhance the spatial resolution of radiometer data," *IEEE Trans. Geosci. Remote Sens.*, vol. 52, no. 5, pp. 2450–2458, May 2014.

[40] W. D. Robinson, C. Kummerow, and W. S. Olson, "A technique for enhancing and matching the resolution of microwave measurements from the SSM/I instrument," *IEEE Trans. Geosci. Remote Sens.*, vol. 30, no. 3, pp. 419–429, May 1992.

[41] M. Migliaccio and A. Gambardella, "Microwave radiometer spatial resolution enhancement," *IEEE Trans. Geosci. Remote Sens.*, vol. 43, no. 5, pp. 1159–1169, May 2005.

[42] E. G. Njoku, J. M. Stacey, and F. T. Barath, "The Seasat scanning multichannel microwave radiometer: Instrument design and performance," *IEEE J. Ocean. Eng.*, vol. OE-5, no. 2, pp. 100–115, Apr. 1980.

[43] M. Sapiano, W. Berg, D. McKague, and C. Kummerow, "Towards an intercalibrated fundamental climate data record of the SSM/I Sensors. *IEEE Trans. Geosci. Remote Sens.*, vol. 51, no. 3, pp. 1492–1503, Mar. 2013.

[44] R. Sethmann, B. A. Burns, and G. C. Heygster, "Spatial resolution improvement of SSM/I data with image restoration techniques," *IEEE Trans. Geosci. Remote Sens.*, vol. 32, no. 6, pp. 1144–1151, Nov. 1994.

[45] C. T. Swift, M. A. Goodberlet, and S. C. Reising, "Antenna pattern synthesis and deconvolution of microwave radiometer imaging data," in *Proc. IEEE MicroRad*, 2006, pp. 216–221.

[46] A. A. Tikhonov and V. Y. Arsenin, *Solution of Ill-Posed Problems*. Washington, DC, USA: Winston & Sons, 1977.

David G. Long (S'80–SM'98–F'08) received the Ph.D. degree in electrical engineering from the University of Southern California, Los Angeles, CA, USA, in 1989.

From 1983 to 1990, he worked for NASA Jet Propulsion Laboratory (JPL), where he developed advanced radar remote sensing systems. While at JPL, he was the Project Engineer on the NASA Scatterometer (NSCAT) project, which flew from 1996 to 1997. He also managed the SCANSCAT project, i.e., the precursor to SeaWinds, which was flown in 1999 on QuikSCAT, in 2002 on ADEOS-II, and in 2014 on the International Space Station. He is currently a Professor with the Department of Electrical and Computer Engineering, Brigham Young University (BYU), Provo, UT, USA, where he teaches the upper division and graduate courses in communications, microwave remote sensing, radar, and signal processing and is the Director of the BYU Center for Remote Sensing. He is the principal investigator on several NASA-sponsored research projects in remote sensing. He has over 400 publications in various areas, including signal processing, radar scatterometry, and synthetic aperture radar. His research interests include microwave remote sensing, radar theory, space-based sensing, estimation theory, signal processing, and mesoscale atmospheric dynamics.

Dr. Long serves as an Associate Editor for IEEE GEOSCIENCE AND REMOTE SENSING LETTERS. He received the NASA Certificate of Recognition several times.

Mary J. Brodzik received the B.A. (*summa cum laude*) degree in mathematics from Fordham University, New York, NY, USA, in 1987.

Since 1993, she has been with the National Snow and Ice Data Center (NSIDC) and with the Cooperative Institute for Research in Environmental Sciences, University of Colorado, Boulder, CO, USA, where she is currently a Senior Associate Scientist. Since coming to NSIDC, she has implemented software systems to design, produce, and analyze snow and ice data products from satellite-based visible and passive microwave imagery. She has contributed to the NSIDC data management and software development teams for the NASA Cold Lands Processes Experiment and Operation IceBridge. As a Principal Investigator on the NASA Making Earth Science Data Records for Use in Research Environments (MEaSUREs) Calibrated Enhanced-Resolution Brightness Temperature project, she is managing the operational production of a 37-year EASE-Grid 2.0 Earth Science Data Record of satellite passive microwave data. She is using MODIS data products to derive the first systematically-derived global map of the world's glaciers. For the U.S. Agency for International Development, she is developing snow and glacier ice melt models to better understand the contribution of glacier ice melt to major rivers with headwaters in High Asia. Her experience includes software development, validation and verification on Defense Department satellite command and control, and satellite tracking systems. Her research interests include optical and passive microwave sensing of snow, remote sensing data gridding schemes, and effective ways to visualize science data.